


JGR Solid Earth

RESEARCH ARTICLE

10.1029/2023JB028026

Thermal Equations of State of Magnesite: Implication for the Complex Mid-Lower Mantle Seismic Scatterers

Yingxin Yu¹ , Ningyu Sun¹, Zhu Mao^{1,2,3} , Luo Li¹ , Vitali B. Prakapenka⁴ , and Jung-Fu Lin⁵ 

¹Deep Space Exploration Laboratory, School of Earth and Space Sciences, University of Science and Technology of China, Hefei, China, ²CAS Center for Excellence in Comparative Planetology, University of Science and Technology of China, Hefei, China, ³Frontiers Science Center for Planetary Exploration and Emerging Technologies, University of Science and Technology of China, Hefei, China, ⁴Center for Advanced Photon Sources, The University of Chicago, Chicago, IL, USA, ⁵Department of Earth and Planetary Sciences, Jackson School of Geosciences, The University of Texas at Austin, Austin, TX, USA

Key Points:

- The velocity change across the MgCO₃-SiO₂ reaction were modeled, with the determined thermal EoS of magnesite up to 120 GPa and 2600 K
- The V_S reduction during the post-stv transition could be influenced by temperature, CO₂ and SiO₂ content, and Al content in SiO₂
- The post-stv transition and the reaction between SiO₂ and MgCO₃ could explain the lower-V_S scatterers at 1,000–1,900 km depth

Supporting Information:

Supporting Information may be found in the online version of this article.

Correspondence to:

Z. Mao and N. Sun,
zhumao@ustc.edu.cn;
ningyu@ustc.edu.cn

Citation:

Yu, Y., Sun, N., Mao, Z., Li, L., Prakapenka, V. B., & Lin, J.-F. (2024). Thermal equations of state of magnesite: Implication for the complex mid-lower mantle seismic scatterers. *Journal of Geophysical Research: Solid Earth*, 129, e2023JB028026. <https://doi.org/10.1029/2023JB028026>

Received 7 OCT 2023
Accepted 17 JAN 2024

Author Contributions:

Data curation: Yingxin Yu, Ningyu Sun, Luo Li, Vitali B. Prakapenka
Formal analysis: Yingxin Yu
Funding acquisition: Ningyu Sun, Zhu Mao
Investigation: Yingxin Yu
Supervision: Zhu Mao
Writing – original draft: Yingxin Yu, Ningyu Sun
Writing – review & editing: Yingxin Yu, Ningyu Sun, Zhu Mao, Jung-Fu Lin

Abstract Magnesite (MgCO₃) entering the lower mantle together with the subducted oceanic crust is an important carbon carrier. The reaction between magnesite and mantle minerals has been documented, but its influence on the density and velocity profiles of lower mantle remains unexplored. To decipher the deep carbon transportation and its associated effect, here we determined the thermal equations of state of magnesite up to 120 GPa and 2600 K using X-ray diffraction in laser-heated diamond anvil cells. The obtained thermal elastic parameters of magnesite facilitated a comprehensive understanding on the influence of magnesite-SiO₂ reaction, variation of carbon and SiO₂ content, and temperature on the origin of lower-mantle scatterers at 1,000–1,800 km depth. Our modeling revealed that the depth of the lower-mantle V_S scatterers is mainly controlled by the Al₂O₃ content in SiO₂, while its magnitude depends on the SiO₂ content. Along normal geotherm, the magnesite-SiO₂ reaction would occur before the post-stishovite transition, consuming substantial SiO₂ in the subducted oceanic crust. Depending on the amount of residual SiO₂, the post-stishovite transition can produce a 2.5–5.2 (2%) V_S reduction, compatible with the observed seismic scatterers in Izu-Bonin and Mariana subduction zones. Along slab geotherm, this reaction occurs after the post-stishovite transition, generating a greater V_S reduction of 4.4–6.4 (4%). We thus propose that the reaction between sinking MgCO₃ and SiO₂ in the slab is one of the potential factors influencing the magnitude of the lower-V_S scatterers at 1,000–1,900 km depth. Our results provide new insights into the deep-mantle carbonate transportation influencing regional geophysics.

Plain Language Summary Carbonates could enter the deep Earth with the subducted oceanic crust. Magnesite is the most likely carbonate to exist stably in the lower mantle. During the subduction process, magnesite would interact with subducted oceanic crust and influence the density and velocity structure of the lower mantle. Here we determined the thermal equations of state (EoS) of magnesite up to 120 GPa and 2600 K. With the obtained EoS parameters, we discussed the influence of magnesite-SiO₂ reaction, variation of carbon, SiO₂ content, and temperature on the velocity and density profiles across the post-stishovite phase transition of SiO₂ and explain the origin of lower-mantle VS scatterers at 1,000–1,900 km depth. Our findings reveal that the depth and magnitude of lower-mantle VS scatterers depend on Al₂O₃ content in SiO₂ and SiO₂ content, respectively. With the variation of temperature and residual SiO₂ content of the reaction, the post-stishovite phase transition of SiO₂ can generate a VS reduction in the range of 2.5%–6.4%. Our findings are important in understanding deep-mantle carbonate transportation and its implications for regional Geophysics.

1. Introduction

The subduction slab is a bridge connecting the Earth's surface and interior (Bekaert et al., 2021). A large amount of surface material, especially volatile components such as carbon and water, will enter the Earth's interior with the sinking of the subduction slab (Bekaert et al., 2021; Dasgupta & Hirschmann, 2010; Walter et al., 2011). During this descent, these carbon and water-containing material continuously degas due to the increasing temperature and pressure (Dasgupta & Hirschmann, 2010). This not only causes partial melting of the overlying mantle wedge, affects the migration and distribution of elements within the Earth's interior, but also reacts with materials in the Earth's interior, leading to lateral heterogeneity in mantle composition (Zheng, 2019). Therefore,

studying the physical properties of materials entering the Earth's interior with subduction slab under high pressure-temperature conditions is of great significance for understanding the circulation of materials in the deep Earth and the mantle lateral composition heterogeneity.

Among various volatile-bearing materials, MgCO_3 is the primary candidate for transporting carbon to the lower mantle via sinking subduction slab (Drewitt et al., 2019; Lv et al., 2021; Maeda et al., 2017). Under ambient conditions, MgCO_3 exists as magnesite with a rhombohedral structure ($R\bar{3}c$) (e.g., Litasov et al., 2008). It was first observed to transition into magnesite-II at 115 GPa and 2200 K (Isshiki et al., 2004). Theoretical calculations indicate that magnesite-II with a $C2/m$ structure is stable between 82 and 138 GPa (Oganov et al., 2008). Although Boulard et al. (2011) synthesized magnesite-II at 82 GPa and 2350 K using $\text{MgO} + \text{CO}_2$, later high-pressure studies did not observe a complete transition from magnesite to magnesite-II until 104 GPa and 3200 K (Binck et al., 2020; Isshiki et al., 2004; Maeda et al., 2017).

Meanwhile, MgCO_3 was reported to react with SiO_2 or davemaoite (CaSiO_3) when it subducted into the mid-lower mantle (Drewitt et al., 2019; Lv et al., 2021; Maeda et al., 2017). For example, prior to transitioning into magnesite-II, magnesite reacts with SiO_2 to form bridgmanite and CO_2 between 40 and 80 GPa with a Clapeyron slope of -74 to -147 MPa/K (Drewitt et al., 2019; Maeda et al., 2017). Residue magnesite will transition into magnesite-II above 80 GPa and 1700 K and further react with SiO_2 to form bridgmanite and diamond (Maeda et al., 2017). A number of small-scale scatterers have been identified at depths of 900–1,900 km with -2% to -12% shear velocity reduction, which were previously proposed to be associated with the structural phase transition of SiO_2 (e.g., Haugland et al., 2017; Hirose et al., 2005; Kaneshima, 2016; Kaneshima, 2019; Li & Yuen, 2014). The reaction between magnesite and SiO_2 in the mid-lower mantle not only consumes magnesite from the subducting oceanic crust but also affects the content of SiO_2 transported from the subducting oceanic crust to the lower mantle. The impact of such reactions on the formation of small-scale seismic scatterers in the mid-lower mantle remains unclear, and further in-depth research on the thermal elastic parameters of magnesite up to lower mantle condition could lead to a deeper understanding of this issue.

Although the physical properties of magnesite have been studied using various experimental techniques, the thermoelastic parameters have only been derived either from experiments at pressures less than 32 GPa up to 2073 K or only under 300 K (Fiquet & Reynard, 1999; Litasov et al., 2008; Redfern et al., 1993; Ross, 1997; Stekiel et al., 2017; Zhang et al., 1997). The isothermal bulk modulus, K_{T0} , determined by previous X-ray diffraction (XRD) experiments at 300 K ranges between 108 and 151 GPa, which exhibits strong tradeoff with its pressure derivative K' of 2.3–4.6 (Litasov et al., 2008; Redfern et al., 1993; Ross, 1997; Zhang et al., 1997). More importantly, the influence of temperature on the density and elasticity of magnesite has been investigated only below 32 GPa (Litasov et al., 2008; Zhang et al., 1997). Extrapolating the density and sound velocity of magnesite determined at low pressures to the relevant pressure conditions of the deep lower mantle would result in large uncertainties.

In this study, we conduct high pressure and temperature (P - T) XRD experiments on magnesite with laser-heated diamond anvil cells (DACs) up to 120 GPa and 2600 K. Using the fitted thermal EoS of magnesite, along with previous experimental data for mantle minerals, we have modeled the density (ρ), shear velocity (V_S), and compressional velocity (V_P) profiles of magnesite. Furthermore, we discussed the influence of the magnesite + SiO_2 reaction on the ρ , V_S and V_P structure of subducted oceanic crust under lower mantle P - T conditions. These modeled density and velocity profiles are used to understand the seismic signature of carbonates and the influence of decarbonation on the seismic profiles along subducting slabs at the depth of mid-lower mantle.

2. Experiments

The natural single-crystal magnesite used in this study was from the Vargas Mineral Collection at the Jackson School of Geosciences, the University of Texas at Austin (Collection number: V3782). The composition of the MgCO_3 sample was examined by electron microprobe analysis, with less than 0.5 mol.% Mn and Fe in total (Yang et al., 2014). XRD measurements under ambient conditions revealed a rhombohedral structure for the sample (space group: $R\bar{3}c$) with a volume of 280.71 \AA^3 (Yang et al., 2014). The sample was ground by agate mortar into fine powder. 5 wt.% Pt was mixed into the sample powder as the heat absorber and pressure calibrant (Fei et al., 2007). The magnesite-Pt mixture was pressed into $\sim 10 \mu\text{m}$ thick foils, and cut into pieces of 40–80 μm afterward. The sample pieces were then sandwiched by two pieces of NaCl or KCl of ~ 5 –7 μm in thickness as the pressure medium and thermal insulator, and Re was used as the gasket material. Experiments below 90 GPa were

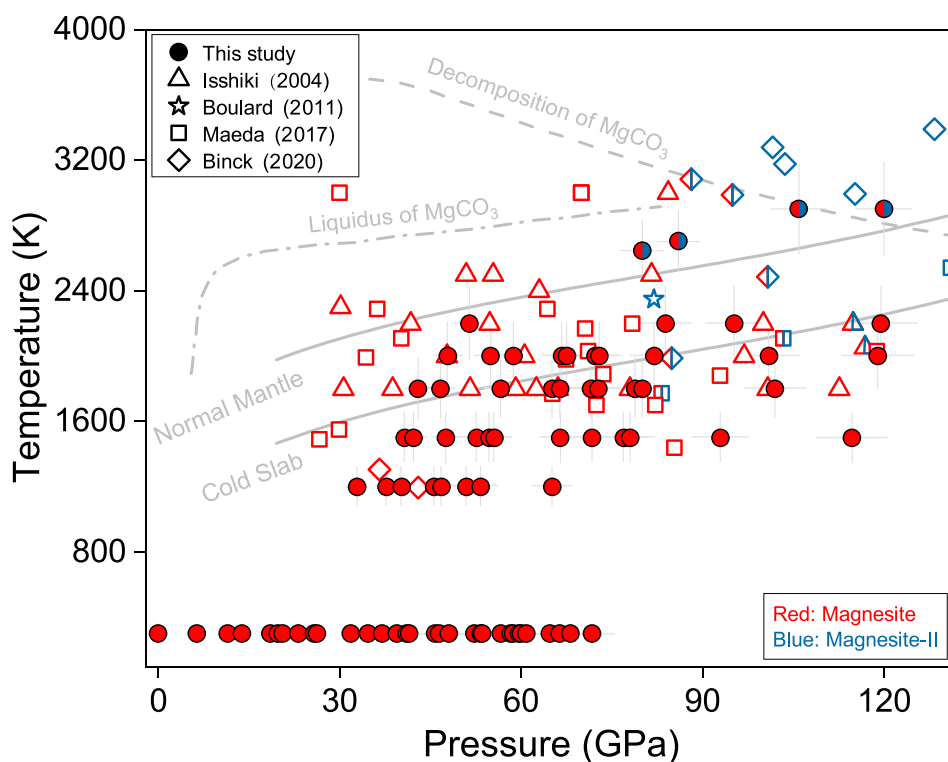


Figure 1. Phase diagram of MgCO_3 at relevant mantle P - T conditions. Red: magnesite; blue: magnesite-II; solid circles: this study; open triangles: Isshiki et al. (2004); open stars: Boulard et al. (2011); open squares: Maeda et al. (2017); open diamonds: Binck et al. (2020); gray dash lines: decomposition lines of MgCO_3 (Fiquet et al., 2002); gray dash-dotted lines: liquidus of MgCO_3 (Solopova et al., 2015); gray solid lines: normal mantle geotherm and a representative cold slab geotherm (500 K lower) (Katsura et al., 2010); open symbol with half red and half blue: coexistence of magnesite and magnesite-II.

performed by using DACs equipped with a pair of 300- μm or 200- μm culet diamonds, while data collected above 90 GPa were obtained by using DACs with two beveled diamonds (150- μm inner culet).

The high P - T XRD experiments were performed at the GeoSoilEnviroConsortium (GSECARS) of the advanced photon source (APS), argonne national laboratory (ANL). The incident X-ray beam with a wavelength of 0.3344 Å was $\sim 3 \times 4 \mu\text{m}$ in size. The sample was initially compressed to ~ 30 GPa at room temperature in which XRD patterns were collected every 2–5 GPa step (Table S1). The sample was heated from both sides (upstream and downstream) using double-sided flat-top infrared lasers, from 30 GPa. The temperature of the heated sample was determined by fitting the collected thermal radiation spectrum with the Planck radiation function under the Graybody approximation (Prakapenka et al., 2008), while pressures of the heated sample were determined by the thermal EoS of Pt (Fei et al., 2007). The temperature uncertainty was $\sim 10\%$ of the measured value by considering the difference in temperature between the upstream and downstream heating sides and the temperature gradient inside the X-ray spot. During each heating cycle between 30 and 120 GPa, XRD patterns were collected at every 200 K from 1200 to 2600 K. XRD patterns were also collected after temperature quenching at high pressure. Dioptas was used to process the XRD data initially and to determine the occurrence of the phase transition (Prescher & Prakapenka, 2015). Origin or Igor program was then used to fit the peak positions, which are used to determine the lattice parameters of magnesite.

3. Result

At temperatures below 2200 K between 33 and 120 GPa, all of our collected XRD patterns can be well interpreted by magnesite, pressure calibrant Pt, and pressure medium KCl (Figures 1, 2 and Figure S2 in Supporting Information S1). The diffraction pattern under 73 GPa and 2000 K was refined using GSAS to confirm the structure of the sample (Figure S2 in Supporting Information S1) (Toby, 2001). Upon heating the sample to 2600 K and 80 GPa, we observed the appearance of new peaks, accompanied by a decrease in the intensity of MgCO_3

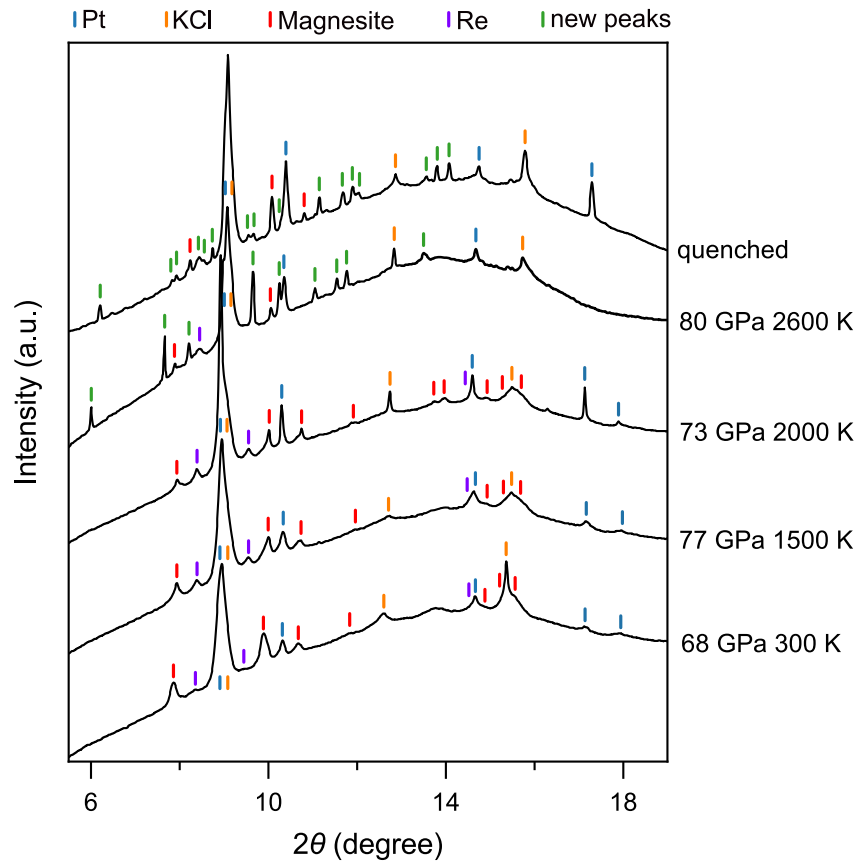


Figure 2. Representative XRD patterns of magnesite at high pressures and temperatures. Black line: diffraction patterns. Vertical ticks indicate the diffraction peak of different material. Blue: Pt; orange: KCl; red: magnesite; purple: Re; green: new peaks appeared after phase transition. Incident X-ray wavelength is 0.3344 Å.

diffraction peaks (Figure 2). As we continued to increase the heating power, a significant laser flash occurred, indicating a rapid transformation. After quenching, the sample was observed to consist of a mixture of magnesite and the newly formed phase. Upon increasing pressure to 120 GPa between 2600 and 3000 K, the XRD patterns were composed of appearance of the new phase together with pressure calibrant and medium (Figure 2). No decomposition or melting of MgCO_3 was observed during all the heating cycles. Calculated deviatoric stress of our sample using collected diffraction patterns of Pt is less than 0.8 GPa at the experimental P-T range (Figure S1 in Supporting Information S1) (Dorfman et al., 2012).

The Pressure-Volume-Temperature (P - V - T) data up to 120 GPa between 300 and 2,200 K were used to constrain the thermal EoS of magnesite (Table S1 in Supporting Information S1, Figures 1 and 3). The P - V - T data was fitted using both third-order isothermal Birch-Murnaghan and Mie-Grüneisen EoS (Table 1). The third-order isothermal Birch-Murnaghan EoS was expressed as:

$$P = \frac{3}{2}K_T \left[\left(\frac{V}{V_0} \right)^{-7/3} - \left(\frac{V}{V_0} \right)^{-5/3} \right] \cdot \left\{ 1 + \frac{3}{4}(K' - 4) \cdot \left[\left(\frac{V}{V_0} \right)^{-2/3} - 1 \right] \right\} \quad (1)$$

The K_T and V_0 would be derived as follows:

$$K_T = K_{T0} + dK_T/dT \times (T - 300) \quad (2)$$

$$V = V_0 \times \exp \left(\int_{300}^T \frac{dK_T}{K_T} \right) \quad (3)$$

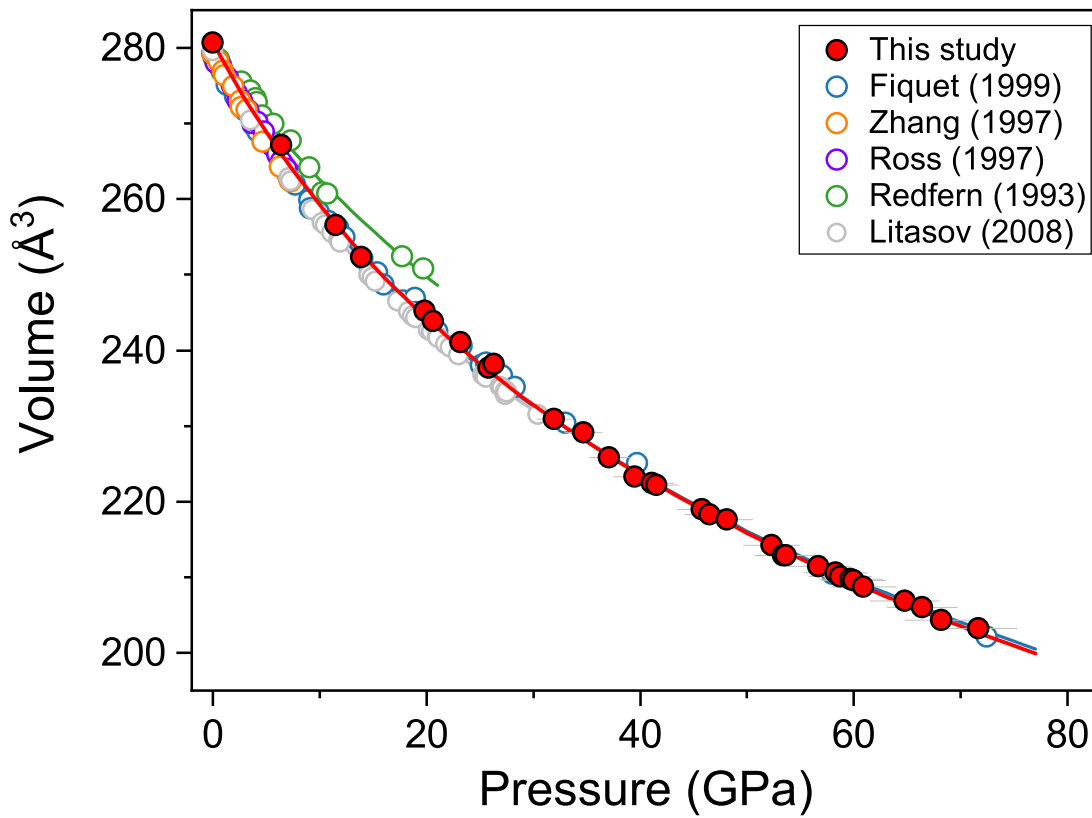


Figure 3. Pressure-volume relationship of magnesite under high pressure and 300 K. Red: this study; blue: Fiquet & Reynard (1999); orange: Zhang et al. (1997); purple: Ross (1997); green: Redfern et al. (1993); gray: Litasov et al. (2008). Error bars are smaller than symbols when not shown.

where K_{T0} and V_0 is the bulk modulus and volume under ambient condition; α is the thermal expansion, and dK_T/dT is the pressure derivative of the bulk modulus.

The Mie-Grüneisen EoS enabled a more reliable extrapolation of the density and velocity profiles beyond the range of the experiments (Jackson & Rigden, 1996). The pressure could be described as

Table 1
Thermal Elastic Parameters of Magnesite

	K_{T0} (GPa)	K_{T0}'	V_0 (Å ³)	θ_0 (K)	γ_0	q	α_0 (*10 ⁻⁵ /K)	α_1 (*10 ⁻⁸ /K)	dK/dT (GPa/K)	P_{max} (GPa)	T_{max} (K)
This study ^a	105 (2)	4.49 (5)	280.71 (fixed)	850 (200)	1.7 (2)	0.9 (3)	--	--	--	119.5	2,200
	107 (2)	4.36 (10)	280.71 (fixed)	--	--	--	4.8 (3)	0.9 (6)	-0.019 (3)	--	--
Zhang et al. (1997) ^b	108 (3)	2.33 (94)	279.27 (13)	--	--	--	3.08	2.3 (3)	-0.017	8.6	1,073
	103 (1)	4 (fixed)	279.27 (13)	--	--	--	3.15	--	-0.021	--	--
Litasov et al. (2008) ^c	97.1 (5)	5.44 (7)	279.55 (2)	--	--	--	4.03 (7)	0.49 (10)	-0.013 (1)	32.2	2,073
	108.4 (4)	4 (fixed)	279.55 (2)	--	--	--	--	--	--	--	--
Fiquet and Reynard (1999) ^d	108 (2)	4.6 (2)	279.1 (1)	--	--	--	--	--	--	72.4	--
Ross (1997)	117 (3)	2.3 (7)	279.28 (3)	--	--	--	--	--	--	6.88	--
	111 (1)	4 (fixed)	279.28 (3)	--	--	--	--	--	--	--	--
Redfern et al. (1993)	151 (7)	2.5 (fixed)	279.4 (2)	--	--	--	--	--	--	19.7	--
	142 (9)	4 (fixed)	279.4 (2)	--	--	--	--	--	--	--	--

^aWith Mie-Grüneisen equations. ^bWith Birch-Murnaghan equations. ^cResult by fitting high P-T data. ^dResult by fitting data at high pressure and 300 K.

$$P = P_c + P_{th} \quad (4)$$

where P_c is the pressure at a reference temperature ($T_0 = 300$ K) from the Birch-Murnaghan EoS (Equation 1), and P_{th} is the thermal pressure caused by increasing temperature. P_{th} is calculated following (Jackson & Rigden, 1996):

$$P_{th}(V, T) = \frac{\gamma}{V} [E_{th}(V, T) - E_{th}(V, T_0)] \quad (5)$$

where E_{th} is the internal thermal energy resulting from the temperature increasing from T_0 to T , and γ is the Grüneisen parameter. E_{th} could be expressed with the Debye temperature, θ_D :

$$E_{th}(V, T) = 9nRT \left(\frac{\theta_D}{T}\right)^{-3} \int_0^{\theta_D/T} \frac{x^3}{e^x - 1} dx \quad (6)$$

where n is the number of atoms of the magnesite formula and R is the gas constant, and the Grüneisen parameter γ could be derived as:

$$\gamma = \gamma_0 \left(\frac{V}{V_0}\right)^q \quad (7)$$

where γ_0 is the Grüneisen parameter at ambient conditions and q is fixed as a constant. θ_D can be calculated as follow:

$$\theta_D = \theta_{D0} \exp\left(-\frac{\gamma - \gamma_0}{q}\right) \quad (8)$$

The fitting residuals with both Birch-Murnaghan and Mie-Grüneisen EoS are shown in Figure S3 of Supporting Information S1 to show the fitting quality of the data.

4. Discussion

The phase transition of magnesite has been the subject of extensive research for years (e.g., Binck et al., 2020; Boulard et al., 2011; Isshiki et al., 2004; Maeda et al., 2017). In this study, we observed the presence of new XRD peaks at 80 GPa when heating magnesite at ~ 2600 K, but we did not observe the complete transition from magnesite to magnesite-II, even at temperatures above 2900 K within the pressure range of 80–120 GPa. Previous studies have also reported a wide coexistence range of magnesite and magnesite-II, extending up to 3100 K, which could be attributed to the limited heating time and the high kinetic energy barrier of the phase transition (Binck et al., 2020; Isshiki et al., 2004; Maeda et al., 2017). Since the motivation of this study was to determine the thermal EoS of magnesite, our heating time here was also limited to less than 5 minutes.

Using the obtained P - V - T data, we compared our measured volume at high pressure and 300 K with previous studies (Figure 3) (Fiquet & Reynard, 1999; Litasov et al., 2008; Redfern et al., 1993; Ross, 1997; Zhang et al., 1997). In general, our measured volumes under high pressure and 300 K are consistent with previous experimental results, except for those in Redfern et al. (1993). Their measured volumes at 10–20 GPa were obviously higher than other studies (Fiquet & Reynard, 1999; Litasov et al., 2008; Ross, 1997; Zhang et al., 1997). The difference could be attributed to the higher deviatoric stress within the methanol-ethanol pressure medium, especially at over 10 GPa in Redfern et al. (1993). Then, we compared the density (ρ) and bulk sound velocity (V_Φ) of magnesite at high pressures and 300 K calculated using reported elastic parameters (Table 1 and Figure 4) (Fiquet & Reynard, 1999; Litasov et al., 2008; Redfern et al., 1993; Ross, 1997; Zhang et al., 1997). Except for Redfern et al. (1993)'s result, below 40 GPa, the difference of ρ and V_Φ in these studies is within 3 (1)% and 6 (1)%, respectively (Fiquet & Reynard, 1999; Litasov et al., 2008; Ross, 1997; Zhang et al., 1997). Redfern et al. (1993)'s result exhibited a lower bulk modulus and smaller density compared to our results and all other studies due to the greater compressibility (Fiquet & Reynard, 1999; Litasov et al., 2008; Ross, 1997; Zhang et al., 1997).

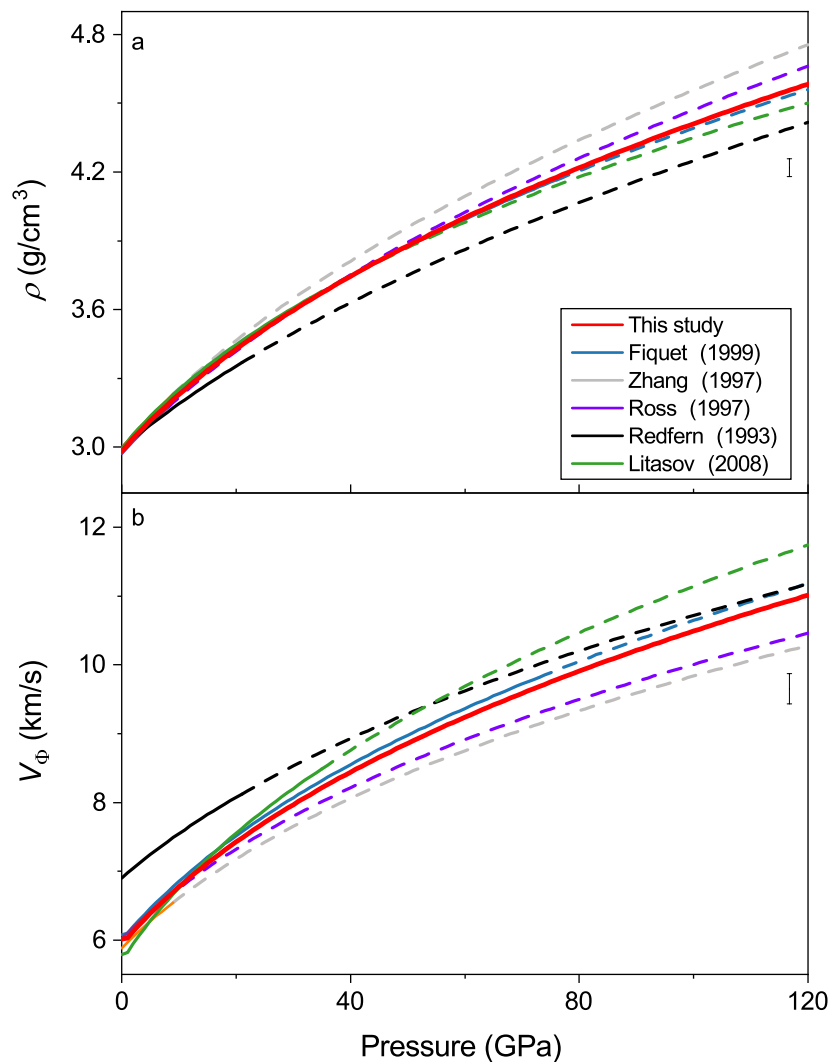


Figure 4. Modeled ρ and V_{ϕ} profiles at high pressures and 300 K. (a) ρ ; (b) V_{ϕ} . Red: this study; blue: Fiquet & Reynard (1999); gray: Zhang et al. (1997); purple: Ross (1997); black: Redfern et al. (1993); green: Litasov et al. (2008). Solid lines: density and velocity within the pressure range of experiments; dash lines: extrapolated results.

At 120 GPa, the density from our study agrees well with Fiquet & Reynard (1999), and the difference in V_{ϕ} is within 0.5 (1%). However, compared with other studies, the difference in the ρ and V_{ϕ} is as large as $\sim 5\%$ and $\sim 10\%$ at 120 GPa, respectively (Litasov et al., 2008; Ross, 1997; Zhang et al., 1997). EoS of magnesite in other studies was constrained using experimental data below 32 GPa (Litasov et al., 2008; Ross, 1997; Zhang et al., 1997). Modeling ρ and V_{ϕ} using these results up to 120 GPa requires significant extrapolation.

To examine the combined effect of pressure and temperature on ρ and V_{ϕ} of magnesite, we modeled them along normal mantle geotherm and 500-K colder slab geotherm, respectively (Figure 5) (Katsura et al., 2010; Litasov et al., 2008; Zhang et al., 1997). Our calculation has revealed that elevating temperature by 500 K can result in a 1.1–1.9 (3)% and 1.3–1.7 (3)% reduction in the ρ and V_{ϕ} at lower-mantle pressures, respectively. Our calculated ρ below 50 GPa, as well as the temperature influence on ρ , aligns well with the findings of Litasov et al. (2008) within the range of calculation uncertainties. However, our ρ demonstrates a stronger dependence on pressure and is 1.6 (2)% higher than that reported by Litasov et al. (2008) at 85 GPa. It is worth noting that the experimental data in Litasov et al. (2008) were obtained at pressures below 32 GPa. A limited pressure range typically results in a larger pressure derivative of the bulk modulus and a lower bulk modulus, which can account for the relatively low ρ at 85 GPa when using the thermal elastic parameters from Litasov et al. (2008). Furthermore, a larger pressure derivative of the bulk modulus and a lower bulk modulus can also result in a greater V_{ϕ} in Litasov

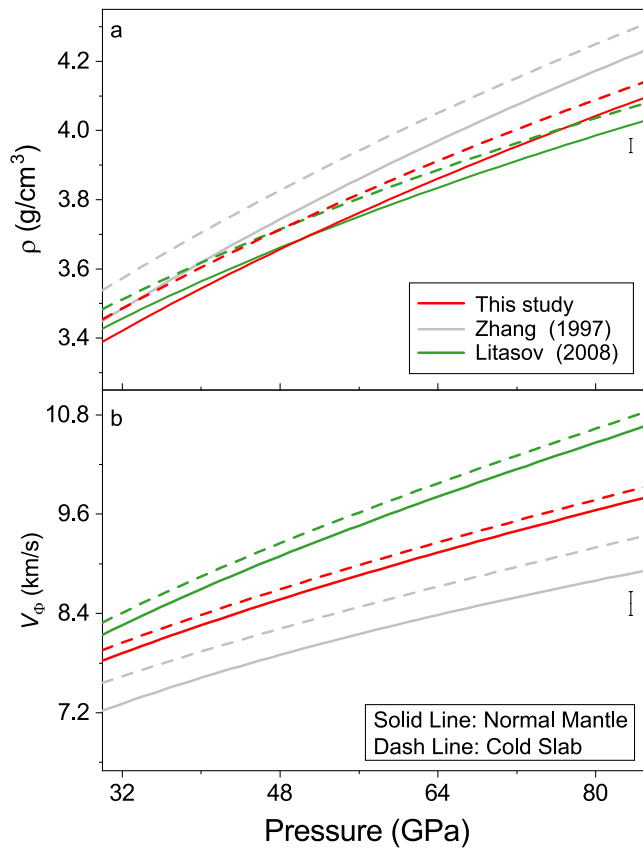


Figure 5. Modeled ρ and V_{ϕ} of magnesite at high pressures and temperatures. (a) ρ ; (b) V_{ϕ} . Red: this study; green: Litasov et al. (2008); gray: Zhang et al. (1997); thick lines: along normal mantle geotherm; thin lines: along a slab geotherm 500 K colder than the normal mantle (Katsura et al., 2010).

et al. (2008) compared to our calculated values. Meanwhile, it is important to highlight that the thermal elastic parameters of magnesite in Zhang et al. (1997) were constrained using experimental data below 8.6 GPa and 1073 K. Calculated ρ and V_{ϕ} using the thermal elastic parameters of Zhang et al. (1997) are significantly different from our results and Litasov et al. (2008).

5. Implication

Seismological studies have observed the existence of numerous scatterers in the Earth's lower mantle at depths ranging from 900 to 1,900 km (e.g., Haugland et al., 2017; Kaneshima & Helffrich, 1999; Niu, 2014; Niu et al., 2003; Zhang et al., 2020). These scatterers exhibit complex seismological structures, with most of them exhibiting a V_S that is 2%–6% lower than that of the normal mantle (e.g., Kaneshima & Helffrich, 1999; Niu, 2014; Niu et al., 2003). In certain regions, such as South America, the magnitude of the low V_S anomaly can even exceed 10% (Haugland et al., 2017). In contrast, the V_P anomalies of these seismic scatterers are less than 1%, and the density anomalies vary between 0.6%–9% (e.g., Kaneshima & Helffrich, 1999; Niu, 2014; Niu et al., 2003; Zhang et al., 2020). Previous studies have proposed that these low-velocity scatterers should be associated with structural phase transitions of SiO_2 in the lower mantle which can produce a significant softening in the V_S (Hirose et al., 2005; Sun et al., 2019; Zhang et al., 2021, 2022). For example, the subducted oceanic crust with 20 vol.% SiO_2 has a V_S 7%–8% lower than the surrounding mantle across the stishovite (stv) to post-stishovite (post-stv) transition (Zhang et al., 2022).

Meanwhile, the variation in the depth of the observed scatterers in the mid-lower mantle could be explained by the varying amounts of Al_2O_3 present in the SiO_2 (Zhang et al., 2022). It has been demonstrated that the addition of 1 mol.% of Al_2O_3 can reduce the transition pressure from stv to post-stv by approximately 30 GPa (~750 km), while 3 mol.% of Al_2O_3 can advance it by around 52 GPa (~1,200 km) along the mantle geotherm (Zhang et al., 2022).

It should be noted that the estimated low V_S anomaly caused by the SiO_2 phase transition in the mid-lower mantle is much larger than the observed 2%–6% values in certain regions at depths of 1,000–1,600 km, such as the Japan Sea and Mariana (Kaneshima & Helffrich, 1999; Niu, 2014). Here, we have conducted a detailed study to investigate the impact of the MgCO_3 - SiO_2 reaction, SiO_2 content, SiO_2 phase transition, and temperature on the density and velocity structure of the subducted oceanic crust. The subducted oceanic crust primarily consists of mid-ocean ridge basalt (MORB). For our modeling, we considered a representative mineral assemblage of MORB, which consists of 39 vol.% bridgmanite, 30 vol.% davemaite, 16 vol.% SiO_2 and 15 vol.% CF-type phase (Hirose et al., 2005; Ishii et al., 2022; Ricolleau et al., 2010). Then, we add 0–5 wt.% CO_2 in the form of MgCO_3 (0–12.1 vol.%) into the MORB as the carbonated oceanic crust and assume a complete reaction between MgCO_3 and SiO_2 (Dasgupta & Hirschmann, 2010). This allows us to evaluate the maximum effect of this reaction on the velocity and density structure of the carbonated oceanic crust. The thermoelastic parameters of the minerals used in the calculations can be found in Table S2 in Supporting Information S1, and the details of the modeling were included in Text S1 of Supporting Information S1. Since the effect of Al content on the V_S reduction across the transition from stv to post-stv is within 3%, and the influence of pressure and temperature on the elasticity of Al-bearing SiO_2 is lacking, we only considered the influence of Al_2O_3 on the depth of SiO_2 phase transition (Zhang et al., 2022).

Along the normal mantle geotherm, ρ , V_P , and V_S of the normal subducted oceanic crust with 16 vol.% SiO_2 are 2.3 (3%), 0.6 (2%), and 0.3 (2%) greater than those of the pyrolitic mantle at ~50 GPa (~1,250 km depth), respectively (Figure 6) (Katsura et al., 2010). Elevating the SiO_2 content from 16 to 25 vol.% can increase the velocity of the subducted oceanic crust by ~1%–2% but rarely change the density (Figures 6 and 7). The difference in sound velocities between the subducted oceanic crust and pyrolitic mantle, particularly for V_S , decreases with increasing depth when SiO_2 approaches the phase transition. V_S of the subducted oceanic crust with

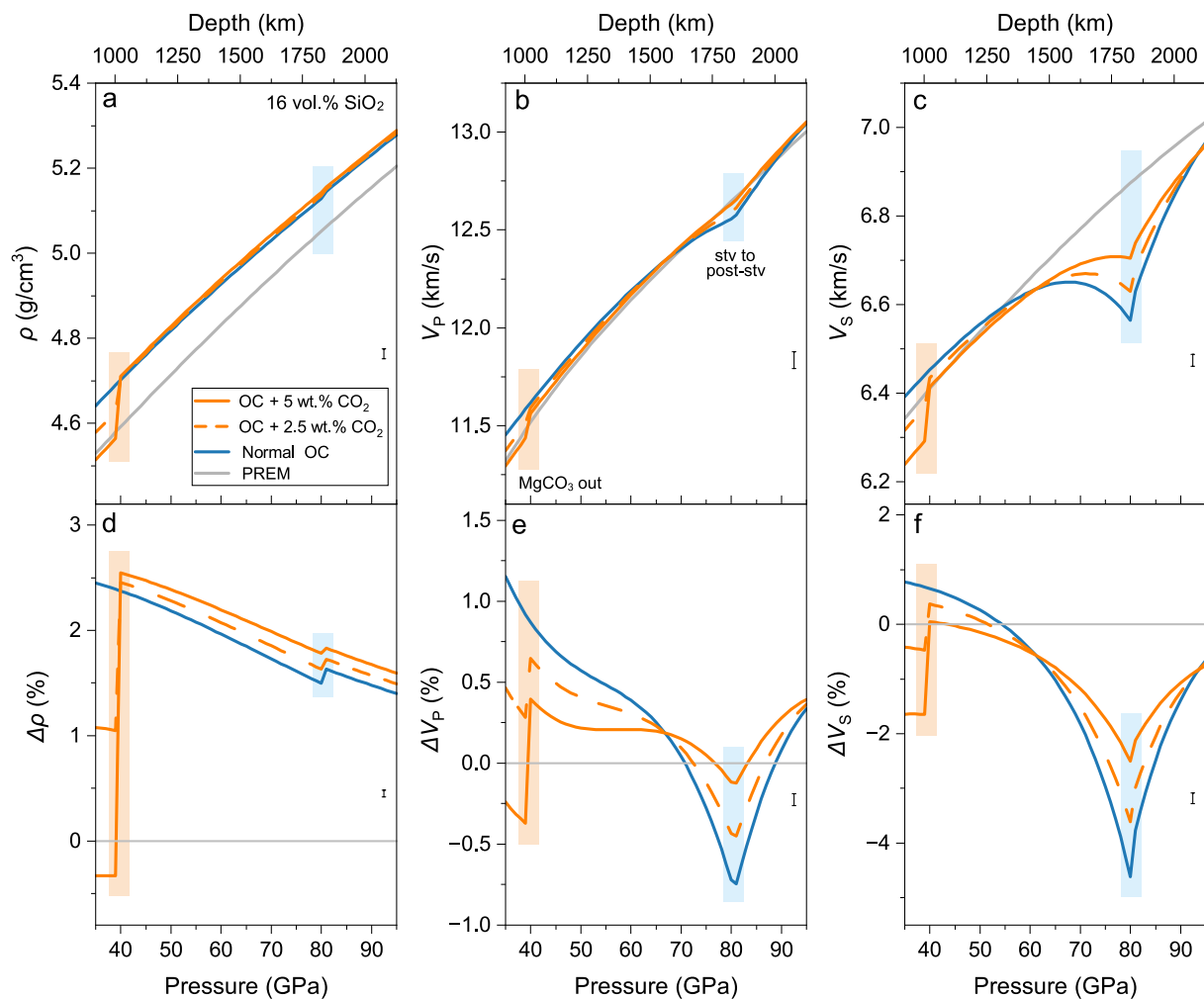


Figure 6. The ρ , V_P , and V_S profiles of subducted oceanic crust with 16 vol.% SiO_2 along the normal mantle geotherm. (a), (b) and (c) are the modeled ρ , V_P , and V_S ; (d), (e) and (f) are the ρ , V_P , and V_S contrasts between normal or carbonated oceanic crust and pyrolitic mantle [$\Delta M = (M_{\text{OC}} - M_{\text{Pyrolitic}})/M_{\text{Pyrolitic}} \times 100\%$] (OC: oceanic crust); orange solid lines: carbonated oceanic crust with 5.0 wt.% CO_2 ; orange dashed lines: carbonated oceanic crust with 2.5 wt.% CO_2 ; blue solid lines: normal oceanic crust; gray solid lines: PREM. Orange shades show the position of the reaction between MgCO_3 and SiO_2 , while blue shades show the pressure range of the phase transition of SiO_2 . Stv: stishovite; post-stv: post-stishovite. Geotherm: from Katsura et al. (2010).

SiO_2 content of 25 vol.% becomes indistinguishable from that of the pyrolitic mantle at ~ 60 GPa ($\sim 1,400$ km depth) considering the calculation uncertainties (Figure 7). The phase transition from stv to post-stv in the subducted oceanic crust produces a pronounced softening in the V_S . When the SiO_2 content is 16 vol.%, the maximum difference in the V_S between the oceanic crust and pyrolitic mantle is 4.6 (3)% across the SiO_2 phase transition. Increasing the SiO_2 content to 25 vol.% in the subducted oceanic crust can enhance the low V_S anomaly to 6.3 (4)% across the SiO_2 phase transition. In contrast, this phase transition exhibits a minor impact on V_P and a negligible effect on ρ (Figures 6 and 7). V_P of oceanic crust is only 0.7%–1.2% lower than the pyrolitic mantle across the SiO_2 phase transition.

Along normal mantle geotherm, the addition of carbon can effectively lower the ρ and sound velocity of the oceanic crust (Katsura et al., 2010). At 16 vol.% SiO_2 content, the presence of 2.5 wt.% CO_2 can lower the ρ , V_P and V_S of oceanic crust by ~ 1.5 (4)%, 0.7 (1)%, and 1.2 (3)% compared to the carbon-free oceanic crust at 35 GPa (~ 950 km), respectively (Figure 6). Increasing the CO_2 content to 5 wt.% makes the ρ and V_P slightly lower than the pyrolitic mantle, and the V_S anomaly reaches up to -1.6 (2)% (Figure 6). The MgCO_3 - SiO_2 reaction along the normal mantle geotherm occurs at ~ 40 GPa ($\sim 1,000$ km), which is shallower than the depth of the post-stishovite transition and will consume large amount of SiO_2 in the subducted oceanic crust (Figure 6) (Katsura et al., 2010;

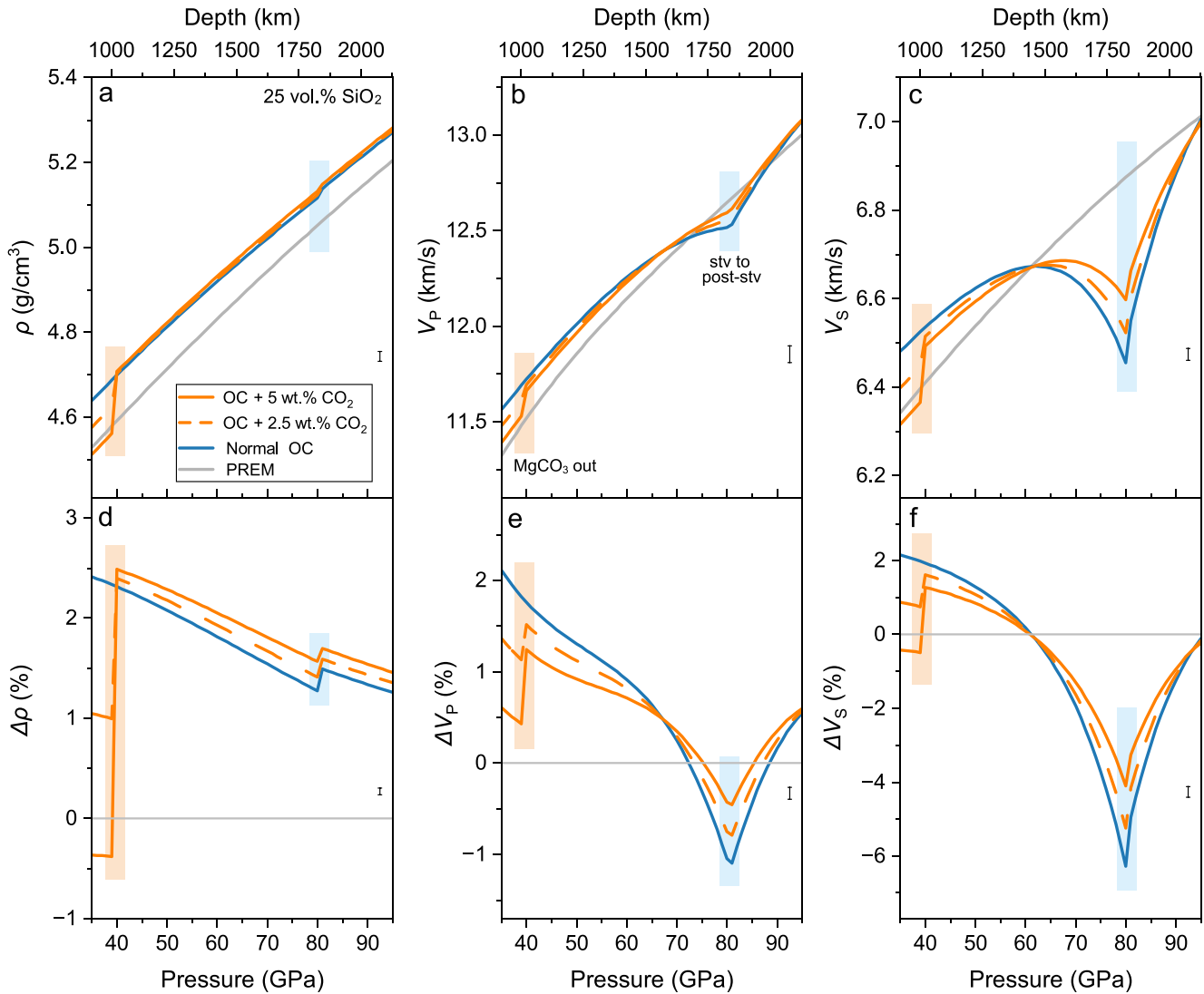


Figure 7. The ρ , V_p , and V_s profiles of subducted oceanic crust with 25 vol.% SiO_2 along the normal geotherm. (a), (b) and (c) are the modeled ρ , V_p , and V_s ; (d), (e) and (f) are the ρ , V_p , and V_s contrasts between normal or carbonated oceanic crust and pyrolitic mantle [$\Delta M = (M_{\text{OC}} - M_{\text{Pyrolite}})/M_{\text{Pyrolite}} \times 100\%$] (OC: oceanic crust); Orange solid lines: carbonated oceanic crust with 5.0 wt.% CO_2 ; orange dashed lines: carbonated oceanic crust with 2.5 wt.% CO_2 ; blue solid lines: normal oceanic crust; gray solid lines: PREM. Orange shades show the position of the reaction between MgCO_3 and SiO_2 , while blue shades show the pressure range of the phase transition of SiO_2 . Stv: stishovite; post-stv: post-stishovite. Geotherm: from Katsura et al. (2010).

Maeda et al., 2017). As a combined effect, the V_p and V_s of the subducted oceanic crust become indistinguishable from the pyrolitic mantle at 40–60 GPa (~1,000–1,450 km) considering calculation uncertainties, while the density is ~2% larger.

The reduction in the SiO_2 content in the subducted oceanic crust due to the MgCO_3 - SiO_2 reaction significantly lowers the magnitude of the V_s softening but has a minor effect on V_p and ρ when stv transitions into post-stv at ~80 GPa (~1,800 km) (Katsura et al., 2010; Zhang et al., 2021). At an initial SiO_2 content of 16 vol.% and CO_2 content of 2.5 wt.%, decarbonated oceanic crust exhibits 0.5 (1%) and 3.5 (4%) lower V_p and V_s , respectively, compared to the pyrolitic mantle at 80 GPa (Figure 6). Elevating the initial CO_2 content to 5 wt.% leads to an increased SiO_2 consumption during the MgCO_3 - SiO_2 reaction. As a result, the low V_s anomaly at 80 GPa is only 2.5 (3%) (Figure 6). With an increased initial SiO_2 content of 25 vol.%, the MgCO_3 - SiO_2 reaction leaves behind 21 to 16 vol.% SiO_2 in the subducted oceanic crust by varying the initial CO_2 content from 2.5 to 5 wt.%. Consequently, the low V_p and V_s anomaly resulting from the post-stishovite transition in the subducted oceanic crust is 0.5–0.8 (1%) and 4.1–5.2 (6%) at 80 GPa, respectively, depending on the initial CO_2 content (Figure 7). It

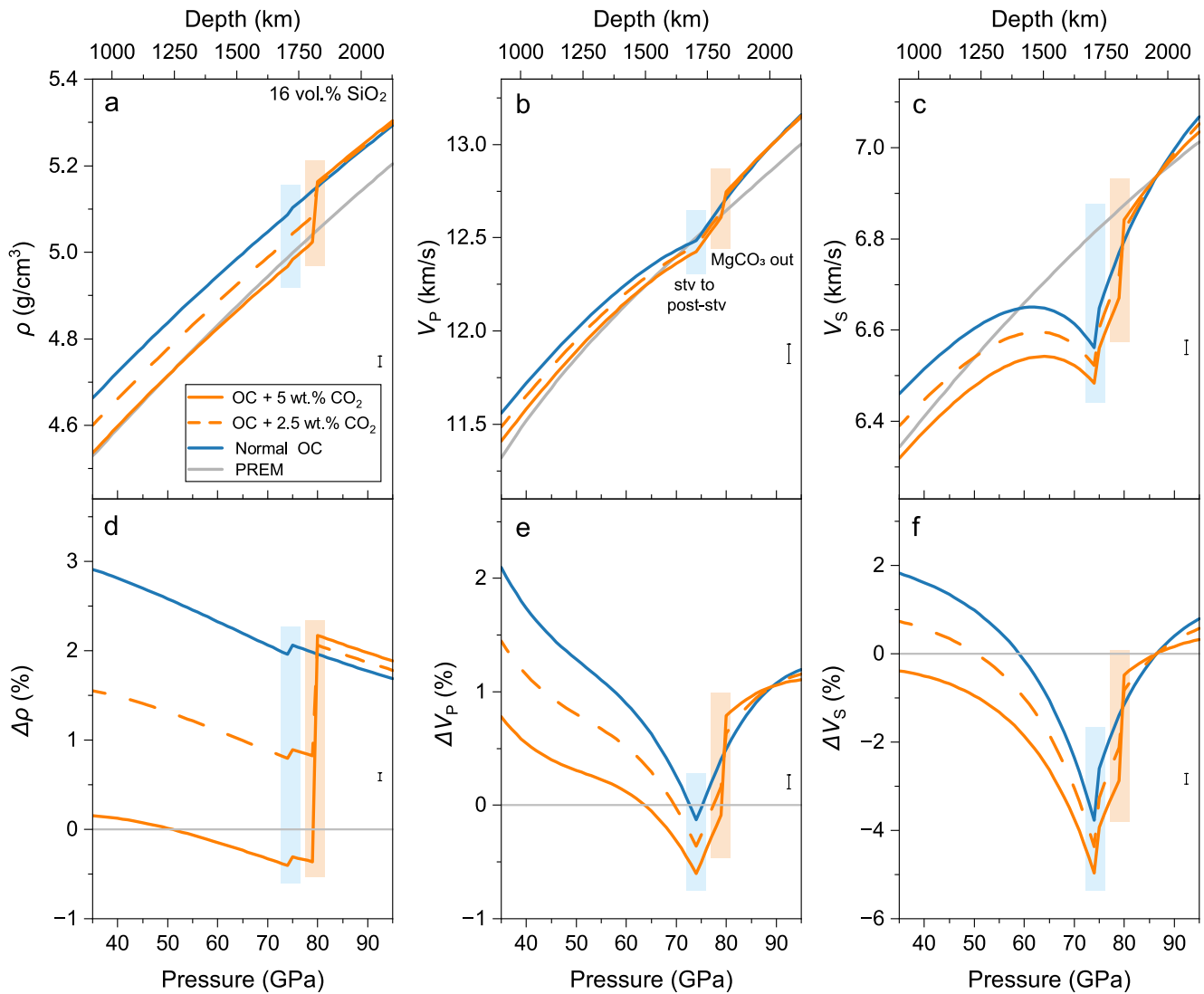


Figure 8. The ρ , V_P , and V_S profiles of subducted oceanic crust with 16 vol.% SiO_2 along a 500-K colder geotherm. (a), (b) and (c) are the modeled ρ , V_P , and V_S ; (d), (e) and (f) are the ρ , V_P , and V_S contrasts between normal or carbonated oceanic crust and pyrolitic mantle [$\Delta M = (M_{\text{OC}} - M_{\text{Pyrolite}})/M_{\text{Pyrolite}} \times 100\%$] (OC: oceanic crust); orange solid lines: carbonated oceanic crust with 5.0 wt.% CO_2 ; orange dashed lines: carbonated oceanic crust with 2.5 wt.% CO_2 ; blue solid lines: normal oceanic crust; gray solid lines: PREM. Orange shades show the position of the reaction between MgCO_3 and SiO_2 , while blue shades show the pressure range of the phase transition of SiO_2 . Stv: stishovite; post-stv: post-stishovite. Geotherm: from Katsura et al. (2010).

is noteworthy that the depth of the post-stishovite transition is strongly influenced by the Al_2O_3 content in SiO_2 (Zhang et al., 2022). Variations in Al_2O_3 content within SiO_2 from 5.2 wt.% to 0 can shift the previously mentioned low V_S anomaly from 1,000 to 1,800 km depth (Figure 9). As a consequence, the combined effect of the MgCO_3 - SiO_2 reaction and Al_2O_3 content in SiO_2 can provide an explanation for the observed 2%–6% low V_S scatterers with a small V_P anomaly in regions such as Japan Sea, Izu-Bonin, and Mariana within the mid-lower mantle between 1,000 and 1,600 km depth (Kaneshima & Helffrich, 1999; Niu, 2014; Niu et al., 2003). Other factors need to be considered to explain up to 9% density anomalies observed in the Mariana subduction zone (Niu et al., 2003).

Meanwhile, the depth of the MgCO_3 - SiO_2 reaction strongly depends on the slab temperature (Drewitt et al., 2019; Maeda et al., 2017). When the temperature of the subducted oceanic crust is ~ 500 K lower than the surrounding mantle, the MgCO_3 - SiO_2 reaction will occur at ~ 74 GPa, which is below the depth of the post-stishovite transition (Drewitt et al., 2019; Maeda et al., 2017) (Figure 8 and Figure S4 in Supporting Information S1). Since the addition of CO_2 will offset the density and sound velocities of the subducted oceanic crust to lower values,

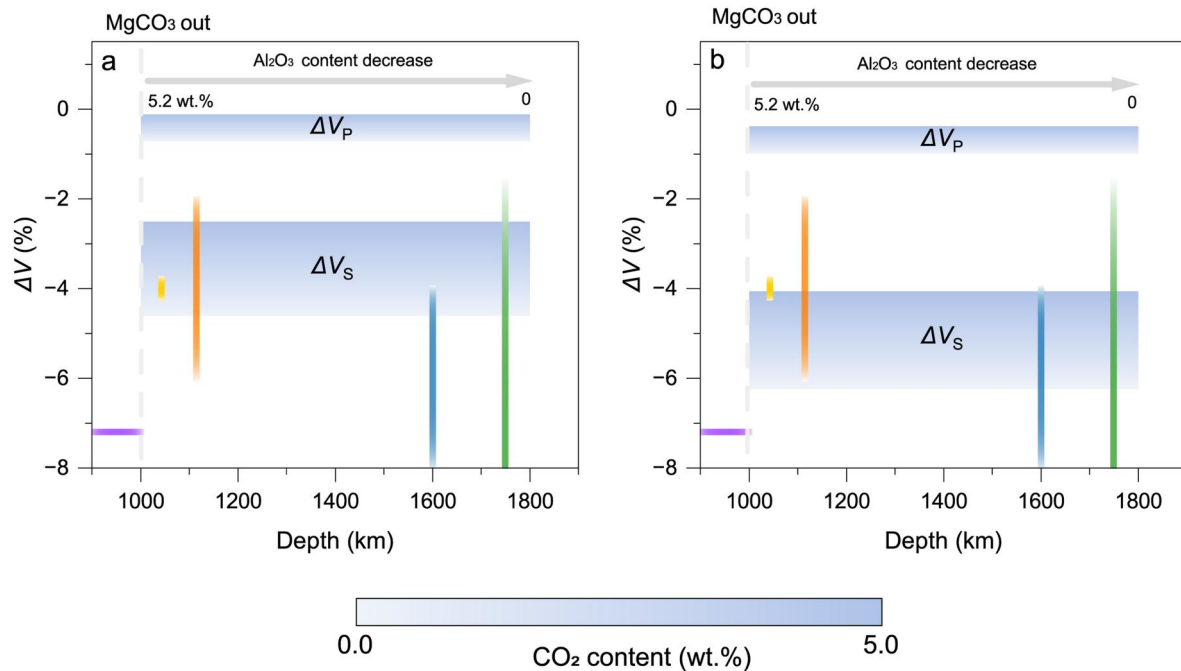


Figure 9. Low V_p and V_s anomalies generated by the carbonated oceanic crust across the post-stishovite phase transition along the normal mantle geotherm. (a) Carbonated oceanic crust with 16 vol.% SiO_2 ; (b) Carbonated oceanic crust with 25 vol.% SiO_2 . Gray arrow: depth of the post-stishovite transition due to the variation of Al_2O_3 content in SiO_2 (Zhang et al., 2021); blue contour: the velocity anomaly due to the post-stishovite transition in the subducted oceanic crust with a variation in the initial CO_2 content from 2.5 to 5.0 wt.%; gray dashed line: depth of the MgCO_3 - SiO_2 reaction along normal mantle geotherm (Drewitt et al., 2019; Maeda et al., 2017). Color vertical bars are the observed seismic low V_s anomalies in the mid-lower mantle. Purple: northeast China (Zhang et al., 2020); yellow: Japan Sea (Niu, 2014); orange: Izu-Bonin (Niu et al., 2003); blue: Mariana (Kaneshima & Helffrich, 1999); green: South America (Haugland et al., 2017).

carbonated oceanic crust with 16–25 vol% SiO_2 and 2.5% CO_2 will have the V_s 4.4–5.9 (7)% lower than the pyrolytic mantle. For a greater initial CO_2 content of 5 wt.%, the low V_s anomaly produced by the post-stishovite transition in the subducted oceanic crust will be as large as 4.9–6.4 (7)% (Figure 8 and Figure S4 in Supporting Information S1).

Our model here provides a detailed analysis of the impact of diverse factors, including carbon content, SiO_2 content, SiO_2 structural phase transitions, and temperature fluctuations within the subducted oceanic crust, on the density and velocity structure of the mid-lower mantle (Figure 9 and Figure S5 in Supporting Information S1). The variations in these factors provide an explanation for the observed small-scale scatterers, featuring varying magnitudes of low V_s anomalies within the mid-lower mantle. We recognized that the low V_s anomalies greater than 7% detected in the regions such as northeast China and South America at depths of 950–1,750 km in the lower mantle cannot be explained by our models (Haugland et al., 2017; Zhang et al., 2020). Since experimental constraints on the influence of Al_2O_3 on the density and velocity of SiO_2 are lacking, whether the formation of these mid-lower mantle low-velocity scatterers is associated with a variation in the Al_2O_3 content within SiO_2 in the subducted oceanic crust or caused by other factors requires further investigation in future studies.

6. Conclusion

In this study, we have determined thermal EoS of magnesite at relevant P - T conditions of the Earth's lower mantle. The phase transition from magnesite to magnesite-II was observed between 80 and 120 GPa above 2600 K, which is consistent with previous studies (Binck et al., 2020; Isshiki et al., 2004; Maeda et al., 2017). Magnesite in the subduction oceanic crust would react with SiO_2 and significantly affect the low V_s anomaly caused by the phase transition of SiO_2 from stv to post-stv. Along a normal mantle geotherm, the magnesite- SiO_2 reaction will occur above the depth of the SiO_2 phase transition. As a result, varying the SiO_2 and CO_2 content in the subducted oceanic crust can lead to a change in the magnitude of the low-velocity anomaly caused by the SiO_2 phase transition from 2.5 to 5.2 (2)%. In contrast, the magnesite- SiO_2 reaction will occur below the depth of the SiO_2 phase transition along a slab geotherm. In this case, the V_s anomaly caused by the SiO_2 phase transition will

be less affected by the magnesite-SiO₂ reaction and would be -4.4--6.4 (4)% depending on the initial SiO₂ and CO₂ content in the subducted oceanic crust. Considering a vary in the Al₂O₃ content on the phase transition depth of SiO₂, the aforementioned low-velocity anomaly can be present between the depth of 1,000 and 1,800 km in the lower mantle, which provided an explanation of low V_s scatterers in various regions of the lower mantle, such as Japan Sea, Izu-Bonin and Mariana (Kaneshima & Helffrich, 1999; Niu, 2014; Niu et al., 2003).

Conflict of Interest

The authors declare no conflicts of interest relevant to this study.

Data Availability Statement

Data used to generate the figures seen in this report can be found in the online supporting information. They can also be downloaded online Yu et al. (2023) (from <https://doi.org/10.5281/zenodo.8399354>).

Acknowledgments

This work is supported by the B-type Strategic Priority Program of the Chinese Academy of Sciences (Grant XDB41000000), National Natural Science Foundation of China (42002037 and 42241117), National Key R&D Program of China (2018YFA0702703), and the Fundamental Research Funds for the Central Universities (WK2080000144). XRD data were collected at GSECARS, supported by the National Science Foundation-Earth Sciences (EAR-1128799). This research used resources of the Advanced Photon Source, a U.S. Department of Energy (DOE) Office of Science User Facility operated for the DOE Office of Science by Argonne National Laboratory under Contract No. DE-AC02-06CH11357. JFL acknowledges support from Geophysics Program of the U.S. National Science Foundation (EAR-1916941 and EAR-2001381).

References

- Bekaert, D., Turner, S., Broadley, M., Barnes, J., Halldórrson, S., Labidi, J., et al. (2021). Subduction-driven volatile recycling: A global mass balance. *Annual Review of Earth and Planetary Sciences*, 49(1), 37–70. <https://doi.org/10.1146/annurev-earth-071620-055024>
- Binck, J., Bayarjargal, L., Lobanov, S. S., Morgenroth, W., Luchitskaia, R., Pickard, C. J., et al. (2020). Phase stabilities of MgCO₃ and MgCO₃-II studied by Raman spectroscopy, x-ray diffraction, and density functional theory calculations. *Physical Review Materials*, 4(5), 055001. <https://doi.org/10.1103/physrevmaterials.4.055001>
- Boulard, E., Gloter, A., Corgne, A., Antonangeli, D., Auzende, A. L., Perrillat, J. P., et al. (2011). New host for carbon in the deep Earth. *Proceedings of the National Academy of Sciences of the United States of America*, 108(13), 5184–5187. <https://doi.org/10.1073/pnas.1016934108>
- Dasgupta, R., & Hirschmann, M. M. (2010). The deep carbon cycle and melting in Earth's interior. *Earth and Planetary Science Letters*, 298(1–2), 1–13. <https://doi.org/10.1016/j.epsl.2010.06.039>
- Dorfman, S. M., Prakapenka, V. B., Meng, Y., & Duffy, T. S. (2012). Intercomparison of pressure standards (Au, Pt, Mo, MgO, NaCl and Ne) to 2.5 Mbar. *Journal of Geophysical Research*, 117(B8). ArtID B08210. <https://doi.org/10.1029/2012jb009292>
- Drewitt, J. W. E., Walter, M. J., Zhang, H. L., McMahon, S. C., Edwards, D., Heinen, B. J., et al. (2019). The fate of carbonate in oceanic crust subducted into earth's lower mantle. *Earth and Planetary Science Letters*, 511, 213–222. <https://doi.org/10.1016/j.epsl.2019.01.041>
- Fei, Y. W., Ricolleau, A., Frank, M., Mibe, K., Shen, G. Y., & Prakapenka, V. (2007). Toward an internally consistent pressure scale. *Proceedings of the National Academy of Sciences of the United States of America*, 104(22), 9182–9186. <https://doi.org/10.1073/pnas.0609013104>
- Fiquet, G., Guyot, F., Kunz, M., Matas, J., Andraut, D., & Hanfland, M. (2002). Structural refinements of magnesite at very high pressure. *American Mineralogist*, 87(8–9), 1261–1265. <https://doi.org/10.2138/am-2002-8-927>
- Fiquet, G., & Reynard, B. (1999). High-pressure equation of state of magnesite: New data and a reappraisal. *American Mineralogist*, 84(5–6), 856–860. <https://doi.org/10.2138/am-1999-5-619>
- Haugland, S. M., Ritsma, J., Kaneshima, S., & Thorne, M. S. (2017). Estimate of the rigidity of eclogite in the lower mantle from waveform modeling of broadband S-to-P wave conversions. *Geophysical Research Letters*, 44(23), 11778–11784. <https://doi.org/10.1002/2017GL075463>
- Hirose, K., Takafuji, N., Sata, N., & Ohishi, Y. (2005). Phase transition and density of subducted MORB crust in the lower mantle. *Earth and Planetary Science Letters*, 237(1–2), 239–251. <https://doi.org/10.1016/j.epsl.2005.06.035>
- Ishii, T., Miyajima, N., Criniti, G., Hu, Q., Glazyrin, K., & Katsura, T. (2022). High pressure-temperature phase relations of basaltic crust up to mid-mantle conditions. *Earth and Planetary Science Letters*, 584, 117472. <https://doi.org/10.1016/j.epsl.2022.117472>
- Isshiki, M., Irifune, T., Hirose, K., Ono, S., Ohishi, Y., Watanuki, T., et al. (2004). Stability of magnesite and its high-pressure form in the lowermost mantle. *Nature*, 427(6969), 60–63. <https://doi.org/10.1038/nature02181>
- Jackson, I., & Rigden, S. M. (1996). Analysis of P-V-T data: Constraints on the thermoelastic properties of high-pressure minerals. *Physics of the Earth and Planetary Interiors*, 96(2–3), 85–112. [https://doi.org/10.1016/0031-9201\(96\)03143-3](https://doi.org/10.1016/0031-9201(96)03143-3)
- Kaneshima, S. (2016). Seismic scatterers in the mid-lower mantle. *Physics of the Earth and Planetary Interiors*, 257, 105–114. <https://doi.org/10.1016/j.pepi.2016.05.004>
- Kaneshima, S. (2019). Seismic scatterers in the lower mantle near subduction zones. *Geophysical Journal International*, 219(Supplement_1), S2–S20. <https://doi.org/10.1093/gji/eggz241>
- Kaneshima, S., & Helffrich, G. (1999). Dipping low-velocity layer in the mid-lower mantle: Evidence for geochemical heterogeneity. *Science*, 283(5409), 1888–1891. <https://doi.org/10.1126/science.283.5409.1888>
- Katsura, T., Yoneda, A., Yamazaki, D., Yoshino, T., & Ito, E. (2010). Adiabatic temperature profile in the mantle. *Physics of the Earth and Planetary Interiors*, 183(1–2), 212–218. <https://doi.org/10.1016/j.pepi.2010.07.001>
- Li, J., & Yuen, D. A. (2014). Mid-mantle heterogeneities associated with Izanagi plate: Implications for regional mantle viscosity. *Earth and Planetary Science Letters*, 385, 137–144. <https://doi.org/10.1016/j.epsl.2013.10.042>
- Litasov, K. D., Fei, Y. W., Ohtani, E., Kuribayashi, T., & Funakoshi, K. (2008). Thermal equation of state of magnesite to 32 GPa and 2073 K. *Physics of the Earth and Planetary Interiors*, 168(3–4), 191–203. <https://doi.org/10.1016/j.pepi.2008.06.018>
- Lv, M., Dorfman, S. M., Badro, J., Borensztajn, S., Greenberg, E., & Prakapenka, V. B. (2021). Reversal of carbonate-silicate cation exchange in cold slabs in Earth's lower mantle. *Nature Communications*, 12(1), 1712. <https://doi.org/10.1038/s41467-021-21761-9>
- Maeda, F., Ohtani, E., Kamada, S., Sakamaki, T., Hirao, N., & Ohishi, Y. (2017). Diamond formation in the deep lower mantle: A high-pressure reaction of MgCO₃ and SiO₂. *Scientific Reports*, 7(1), 40602. <https://doi.org/10.1038/srep40602>
- Niu, F. L. (2014). Distinct compositional thin layers at mid-mantle depths beneath northeast China revealed by the USArray. *Earth and Planetary Science Letters*, 402, 305–312. <https://doi.org/10.1016/j.epsl.2013.02.015>
- Niu, F. L., Kawakatsu, H., & Fukao, Y. (2003). Seismic evidence for a chemical heterogeneity in the midmantle: A strong and slightly dipping seismic reflector beneath the Mariana subduction zone. *Journal of Geophysical Research*, 108(B9). <https://doi.org/10.1029/2002jb002384>

- Oganov, A. R., Ono, S., Ma, Y. M., Glass, C. W., & Garcia, A. (2008). Novel high-pressure structures of MgCO_3 , CaCO_3 and CO_2 and their role in Earth's lower mantle. *Earth and Planetary Science Letters*, 273(1–2), 38–47. <https://doi.org/10.1016/j.epsl.2008.06.005>
- Prakapenka, V. B., Kubo, A., Kuznetsov, A., Laskin, A., Shkurikhin, O., Dera, P., et al. (2008). Advanced flat top laser heating system for high pressure research at GSECARS: Application to the melting behavior of germanium. *High Pressure Research*, 28(3), 225–235. <https://doi.org/10.1080/08957950802050718>
- Prescher, C., & Prakapenka, V. B. (2015). DIOPTAS: A program for reduction of two-dimensional X-ray diffraction data and data exploration. *High Pressure Research*, 35(3), 223–230. <https://doi.org/10.1080/08957959.2015.1059835>
- Redfern, S. A. T., Wood, B. J., & Henderson, C. M. B. (1993). Static compressibility of magnesite to 20 GPa - implications for MgCO_3 in the lower mantle. *Geophysical Research Letters*, 20(19), 2099–2102. <https://doi.org/10.1029/93gl02507>
- Ricolleau, A., Perrillat, J. P., Fiquet, G., Daniel, I., Matas, J., Addad, A., et al. (2010). Phase relations and equation of state of a natural MORB: Implications for the density profile of subducted oceanic crust in the Earth's lower mantle. *Journal of Geophysical Research*, 115(B8). <https://doi.org/10.1029/2009JB006709>
- Ross, N. L. (1997). The equation of state and high-pressure behavior of magnesite. *American Mineralogist*, 82(7–8), 682–688. <https://doi.org/10.2138/am-1997-7-805>
- Solopova, N. A., Dubrovinsky, L., Spivak, A. V., Litvin, Y. A., & Dubrovinskaya, N. (2015). Melting and decomposition of MgCO_3 at pressures up to 84 GPa. *Physics and Chemistry of Minerals*, 42(1), 73–81. <https://doi.org/10.1007/s00269-014-0701-1>
- Stekiel, M., Tra, N. T., Chariton, S., McCammon, C., Bosak, A., Morgenroth, W., et al. (2017). High pressure elasticity of FeCO_3 - MgCO_3 carbonates. *Physics of the Earth and Planetary Interiors*, 271, 57–63. <https://doi.org/10.1016/j.pepi.2017.08.004>
- Sun, N. Y., Shi, W. G., Mao, Z., Zhou, C. J., & Prakapenka, V. B. (2019). High pressure-temperature study on the thermal equations of state of seifertite and CaCl_2 -type SiO_2 . *Journal of Geophysical Research*, 124(12), 12620–12630. <https://doi.org/10.1029/2019JB017853>
- Toby, B. H. (2001). EXPGUI, a graphical user interface for GSAS. *Journal of Applied Crystallography*, 34(2), 210–213. <https://doi.org/10.1107/s0021889801002242>
- Walter, M., Kohn, S., Araujo, D., Bulanova, G., Smith, C., Gaillou, E., et al. (2011). Deep mantle cycling of oceanic crust: Evidence from diamonds and their mineral inclusions. *Science*, 334(6052), 54–57. <https://doi.org/10.1126/science.1209300>
- Yang, J., Mao, Z., Lin, J. F., & Prakapenka, V. B. (2014). Single-crystal elasticity of the deep-mantle magnesite at high pressure and temperature. *Earth and Planetary Science Letters*, 392, 292–299. <https://doi.org/10.1016/j.epsl.2014.01.027>
- Yu, Y., Sun, N., Mao, Z., Li, L., Prakapenka, V. B., & Lin, J.-F. (2023). Thermal equations of state of magnesite: Implication for the complex mid-lower mantle seismic scatterers (version 2) [Dataset]. Zenodo, <https://doi.org/10.5281/zenodo.8399354>
- Zhang, J., Martinez, I., Guyot, F., Gillet, P., & Saxena, S. K. (1997). X-ray diffraction study of magnesite at high pressure and high temperature. *Physics and Chemistry of Minerals*, 24(2), 122–130. <https://doi.org/10.1007/s002690050025>
- Zhang, L. M., Li, J., Wang, T., Yang, F., & Chen, Q. F. (2020). Body waves retrieved from noise cross-correlation reveal lower mantle scatterers beneath the northwest pacific subduction zone. *Geophysical Research Letters*, 47(19), e2020GL2088. <https://doi.org/10.1029/2020GL088846>
- Zhang, Y. Y., Fu, S. Y., Karato, S. I., Okuchi, T., Chariton, S., Prakapenka, V. B., & Lin, J. F. (2022). Elasticity of hydrated Al-bearing stishovite and post-stishovite: Implications for understanding regional seismic V-S anomalies along subducting slabs in the lower mantle. *Journal of Geophysical Research*, 127(4), e2021JB023170. ARTN e2021JB023170. <https://doi.org/10.1029/2021JB023170>
- Zhang, Y. Y., Fu, S. Y., Wang, B. Y., & Lin, J. F. (2021). Elasticity of a pseudoproper ferroelastic transition from stishovite to post-stishovite at high pressure. *Physical Review Letters*, 126(2), 025701. <https://doi.org/10.1103/physrevlett.126.025701>
- Zheng, Y.-F. (2019). Subduction zone geochemistry. *Geoscience Frontiers*, 10(4), 1223–1254. <https://doi.org/10.1016/j.gsf.2019.02.003>

References From the Supporting Information

- Cottaar, S., Heister, T., Rose, I., & Unterborn, C. (2014). BurnMan: A lower mantle mineral physics toolkit. *Geochemistry, Geophysics, Geosystems*, 15(4), 1164–1179. <https://doi.org/10.1002/2013gc005122>
- Dai, L. D., Kudo, Y., Hirose, K., Murakami, M., Asahara, Y., Ozawa, H., et al. (2013). Sound velocities of $\text{Na}_{0.4}\text{Mg}_{0.6}\text{Al}_{1.6}\text{Si}_{0.4}\text{O}_4$ NAL and CF phases to 73 GPa determined by Brillouin scattering method. *Physics and Chemistry of Minerals*, 40(3), 195–201. <https://doi.org/10.1007/s00269-012-0558-0>
- Fei, Y., & Ahrens, T. (1995). Thermal expansion. *Mineral physics and crystallography: a handbook of physical constants*, 2, 29–44.
- Fiquet, G., Dewaele, A., Andrault, D., Kunz, M., & Le Bihan, T. (2000). Thermoelastic properties and crystal structure of MgSiO_3 perovskite at lower mantle pressure and temperature conditions. *Geophysical Research Letters*, 27(1), 21–24. <https://doi.org/10.1029/1999gl008397>
- Fiquet, G., & Reynard, B. (1999). High-pressure equation of state of magnesite: New data and a reappraisal. *American Mineralogist*, 84(5–6), 856–860. <https://doi.org/10.2138/am-1999-5-619>
- Greaux, S., Irifune, T., Higo, Y., Tange, Y., Arimoto, T., Liu, Z. D., & Yamada, A. (2019). Sound velocity of CaSiO_3 perovskite suggests the presence of basaltic crust in the Earth's lower mantle. *Nature*, 565(7738), 218–221. <https://doi.org/10.1038/s41586-018-0816-5>
- Helffrich, G., Ballmer, M. D., & Hirose, K. (2018). Core-exsolved SiO_2 dispersal in the Earth's mantle. *Journal of Geophysical Research: Solid Earth*, 123(1), 176–188. <https://doi.org/10.1002/2017jb014865>
- Hill, R. (1952). The elastic behaviour of a crystalline aggregate. *Proceedings of the Physical Society Section A*, 65(5), 349–354. <https://doi.org/10.1088/0370-1298/65/5/307>
- Imada, S., Hirose, K., Komabayashi, T., Suzuki, T., & Ohishi, Y. (2012). Compression of $\text{Na}_{0.4}\text{Mg}_{0.6}\text{Al}_{1.6}\text{Si}_{0.4}\text{O}_4$ NAL and Ca-ferrite-type phases. *Physics and Chemistry of Minerals*, 39(7), 525–530. <https://doi.org/10.1007/s00269-012-0508-x>
- Kiefer, B., Stixrude, L., & Wentzcovitch, R. (2002). Elasticity of (Mg, Fe) SiO_3 -perovskite at high pressures. *Geophysical Research Letters*, 29(11), 31–34. <https://doi.org/10.1029/2002gl014683>
- Ross, N. L. (1997). The equation of state and high-pressure behavior of magnesite. *American Mineralogist*, 82(7–8), 682–688. <https://doi.org/10.2138/am-1997-7-805>
- Shim, S.-H., & Duffy, T. S. (2000). Constraints on the PVT equation of state of MgSiO_3 perovskite. *American Mineralogist*, 85(2), 354–363. <https://doi.org/10.2138/am-2000-2-314>
- Sinogeikin, S. V., Zhang, J., & Bass, J. D. (2004). Elasticity of single crystal and polycrystalline MgSiO_3 perovskite by Brillouin spectroscopy. *Geophysical Research Letters*, 31(6). <https://doi.org/10.1029/2004gl019559>
- Smyth, J. R., & McCormick, T. C. (1995). Crystallographic data for minerals. In *Mineral Physics and Crystallography: A Handbook of Physical Constants* (Vol. 2, pp. 1–17).
- Stixrude, L., & Lithgow-Bertelloni, C. (2005). Thermodynamics of mantle minerals—I. Physical properties. *Geophysical Journal International*, 162(2), 610–632. <https://doi.org/10.1111/j.1365-246x.2005.02642.x>

- Sun, N., Mao, Z., Yan, S., Wu, X., Prakapenka, V. B., & Lin, J. F. (2016). Confirming a pyrolytic lower mantle using self-consistent pressure scales and new constraints on CaSiO₃ perovskite. *Journal of Geophysical Research: Solid Earth*, *121*(7), 4876–4894. <https://doi.org/10.1002/2016jb013062>
- Tsuchiya, T., Tsuchiya, J., Umemoto, K., & Wentzcovitch, R. M. (2004). Phase transition in MgSiO₃ perovskite in the earth's lower mantle. *Earth and Planetary Science Letters*, *224*(3–4), 241–248. <https://doi.org/10.1016/j.epsl.2004.05.017>
- Wang, F. L., Tange, Y., Irifune, T., & Funakoshi, K. (2012). P-V-T equation of state of stishovite up to mid-lower mantle conditions. *Journal of Geophysical Research: Solid Earth*, *117*(B6). <https://doi.org/10.1029/2011JB009100>
- Xu, W., Lithgow-Bertelloni, C., Stixrude, L., & Ritsema, J. (2008). The effect of bulk composition and temperature on mantle seismic structure. *Earth and Planetary Science Letters*, *275*(1–2), 70–79. <https://doi.org/10.1016/j.epsl.2008.08.012>